

Article

# Electrical Machine Winding Performance Optimization by Multi-Objective Particle Swarm Algorithm

François S. Martins <sup>\*</sup>, Bernardo P. Alvarenga <sup>†</sup> and Geyverson T. Paula <sup>†</sup>

School of Electrical, Mechanical and Computing Engineering, Federal University of Goiás, Av. Universitária, 1488, Goiânia 74605-010, Brazil; bernardo\_alvarenga@ufg.br (B.P.A.); geyverson@ufg.br (G.T.P.)

\* Correspondence: francoissouza@discente.ufg.br

<sup>†</sup> These authors contributed equally to this work.

**Abstract:** The present work aims to optimize the magnetomotive force and the end-winding leakage inductance from a discrete distribution of conductors in electrical machines through multi-objective particle swarm heuristics. From the development of an application capable of generating the conductor distribution for different machine configurations (single or poly-phase, single or double layer, integral or fractional slots, full or shortened pitch, with the presence of empty slots, etc.) the curves of magnetomotive force and the end-winding leakage inductance associated with the winding are computed. Taking as an optimal winding the one that presents, simultaneously, less harmonic distortion of the magnetomotive force and less leakage inductance, optimization by multi-objective particle swarm was used to obtain the optimal electrical machine configuration and the results are presented.

**Keywords:** magnetomotive force; winding optimization; particle swarm; multi-objective optimization



**Citation:** Martins, F.S.; Alvarenga, B.P.; Paula, G.T. Electrical Machine Winding Performance Optimization by Multi-Objective Particle Swarm Algorithm. *Energies* **2024**, *17*, 2286. <https://doi.org/10.3390/en17102286>

Academic Editors: Gang Lei, Youguang Guo and Xin Ba

Received: 17 March 2024

Revised: 9 April 2024

Accepted: 22 April 2024

Published: 9 May 2024



**Copyright:** © 2024 by the authors. Licensee MDPI, Basel, Switzerland. This article is an open access article distributed under the terms and conditions of the Creative Commons Attribution (CC BY) license (<https://creativecommons.org/licenses/by/4.0/>).

## 1. Introduction

One of the main concerns in the design of electrical machines is centered on the correct determination of the constructive parameters of the windings, aiming at minimizing the existing harmonic content in the waveform of the air gap magnetomotive force.

The existence of harmonics in the magnetomotive force curve leads to a decrease in the machine performance, caused by current and parasitic fluxes, an increase in losses in copper and iron, an increase in magnetic saturation, mechanical vibrations, and noise [1–4]. Furthermore, there are changes in torque and speed performance, since the magnetomotive force is distorted from a purely sinusoidal wave [5–7].

On the other hand, in asynchronous machines, for example, characteristics such as starting torque, maximum torque, rotor currents, and stator currents are intrinsically linked to the leakage inductance presented by the machine [8–10]. These characteristics directly affect the performance of motors and generators and their applicability, as well as the materials used for their construction, with the optimization of these effects being of financial and energetic interest.

There are four main topology optimization techniques concerned with improving the material distribution of the rotor and stator: ON–OFF, as used in [11–14]; bi-directional evolutionary structural optimization (BESO), shown in [15–17]; solid-isotropic material with penalization (SIMP), as in [18,19]; and the level set, applied in [20–22]. These techniques are used to maximize the average torque, minimize the ripple or cogging torque, or minimize the weight of the machines but there are challenges to the manufacturability of the optimized topologies when the final geometries are highly irregular.

Despite a vast literature on optimizing stator windings for common machine types (three-phase and single-phase), e.g., [11,23,24], there remains a critical need to explore unconventional configurations. Existing research on air gap MMF curve optimization, such as the work by Marault et al. [25] focusing on specific harmonics, demonstrates the potential of optimization techniques. However, these techniques often target common machine types

and struggle with limitations. Bekka et al. [26] used genetic algorithms but were limited to three-phase machines, while Franco et al. [4] expanded the genetic algorithm optimization solution to poly-phase machines, which faced increased computational burden due to testing infeasible windings.

There remains a critical need to explore unconventional machine configurations and their refined optimization for the development of novel applications. Current research suffers from a lack of studies dedicated to less common typologies, particularly for reduced systems. Optimizing these unconventional windings is often a laborious task. Traditional methods necessitate the exhaustive evaluation of all possible configurations, leading to significant computational burden that renders such approaches impractical. Therefore, there exists a critical need to develop novel tools capable of optimizing a vast array of parameters within the winding construction process, independent of established topological constraints.

This work aims to create an application capable of analyzing the main performance characteristics of the windings and finding the best alternatives for winding construction, trying to avoid a high computational cost.

## 2. Materials and Methods

### 2.1. Winding Design for Alternating Current Electric Machines

#### 2.1.1. Machine Windings Characteristics

Types of windings:

- Lap winding: The lap winding is constructed by connecting adjacent coils in series. Each coil has two sides. The coils are mounted in such a way that each coil is placed on top of the previous one, but under the next one. This configuration allows for greater ease of construction in either single or double layers since the coils have the same size and geometry. Furthermore, it is simple to perform short-pitching [27–29].
- Wave winding: The wave winding is mounted in such a way that the sides of successive “coils” are connected in series. Therefore, one “coil” performs a complete “turn” (wave) along the circumference of the air gap [27–29].
- Concentric winding: Concentric winding differs from the others by having coils of different sizes. Each pole of each phase has a set of coils that share the same axis of symmetry. In some cases, the spread of the phase winding is limited to one polar pitch [27–29].

Number of phases:

- Normal systems: These have an odd number of phases ( $m = 1, 3, 5, 7, \dots$ ) not showing neutral point asymmetry loading, except for  $m = 1$  [28].
- Reduced systems: These have neutral point asymmetry loading ( $m = 2, 4, 6, \dots$ ) [28].
- Non-reduced systems: These combine previous systems, not showing neutral point asymmetry [28].

Coil pitch: Coil pitch is obtained from the number of slots or the distance between the sides of a coil. It is defined as the ratio between the coil pitch and pole pitch. Windings that have unity coil pitch are called full-pitch windings. On the other hand, if the coil pitch is less or greater than unity, the winding is said to be of shortened-pitch or increased-pitch, respectively.

Number of layers:

- In single-layer windings, each slot holds only one coil side, so the number of coils is half the number of slots. Thus, in the cases of wave and lap windings, the coil pitch is always full [27–29].
- In double-layer windings, each slot holds two sides of coils, so the number of coils is equal to the number of slots. Thus, there is a freedom in choosing the coil pitch [27–29].

Distribution of conductors:

- Integral windings are characterized by having the same number of conductors for each pole and phase, being symmetrical. This type of winding has an electric period equal to twice the polar pitch [27–29].
- Fractional windings have a number of slots per pole and phase that is represented by a fraction. In this case, in order to accommodate the coils, it is necessary to use more than one electric period [27–29].

### 2.1.2. Feasibility Conditions and Symmetry

Feasibility conditions: As described by Jokinen et al. [28] and Caruso et al. [30], to obtain feasible windings the number of coils per phase must be an integer. This is accomplished when the number of slots of the winding satisfies condition (1):

$$n_{lay} \cdot \frac{Z - n_{es}}{2m} \in \mathbb{N} \quad (1)$$

where  $Z$  is the number of slots,  $n_{lay}$  is the number of layers,  $m$  is the number of phases, and  $n_{es}$  is the number of empty slots.

The phase span angle  $\alpha_{ph}$  must be an integer multiple of the angle between phasors of individual sides of the coil electromotive force (EMF) in the slots  $\alpha_Z$ . Therefore:

- For normal or non-reduced systems:

$$\frac{\alpha_{ph}}{\alpha_Z} = \frac{2\pi/m}{2\pi t'/Z} = \frac{Z}{mt'} \in \mathbb{N} \quad (2)$$

- For reduced systems:

$$\frac{\alpha_{ph}}{\alpha_Z} = \frac{Z}{2mt'} \in \mathbb{N} \quad (3)$$

where  $t'$  is defined by

$$t' = \text{gcd}(Z, p) \quad (4)$$

which defines the number of repeating structures of the winding.

Therefore, the number of slots in one repeating structure of the winding is given by  $Z/t'$ .

Once the choice of machine winding design parameters satisfy the conditions described in Equations (1)–(3), feasibility of the winding is achieved.

Symmetry conditions: The symmetry of a winding can be checked using the phasor diagram [30]. Each coil generates two electromotive force (EMF) phasors associated with a shift angle according to its geometric position and the number of existing subsystems for this winding. By carrying out the vector sum of the contributions of the phasors of the individual coils of the same phase, the resulting voltage phasor is obtained.

The winding for which the resulting phase voltage phasors have the same magnitude and with the same shift angles between them is said to be symmetrical, for this coil distribution generates a symmetrical phasor diagram.

In order to illustrate this idea, consider a three-phase single-layer winding induction motor with  $Z = 24$  slots and  $2p = 4$  poles. From (4),

$$t' = \text{gcd}(24, 2) = 2 \text{ repeating structures.}$$

Therefore, there are 2 overlapping EMF sub-diagrams, each of them is formed by  $Z' = Z/t' = 12$  phasors shifted one from the other by the electrical angle  $\alpha$ , as per Equation (5):

$$\alpha = \frac{2\pi}{Z/t'} = 2 \cdot \frac{2\pi}{24} = 0.5236 \text{ rad, or } 30 \text{ deg} \quad (5)$$

Each slot is associated with an electrical angle  $\phi_k$  according to Equation (6):

$$\phi_k = k \cdot \alpha \quad (6)$$

where  $k = 0, 1, 2, \dots, Z' - 1$ .

For the example winding, the conductor distribution diagram is shown in Figure 1, which demonstrates the phase coil allocation and corresponding current direction.

The current direction determines the direction of the phasor EMF generated by each side of the coil. For the formation of the phasor diagram, the EMF contribution of the allocated conductor for each slot is calculated. In this work, coils are always assumed to have the same number of turns. Therefore, EMF contributions are always of the same amplitude.

1	2	3	4	5	6	7	8	9	10	11	12	13	14	15	16	17	18	19	20	21	22	23	24
1	1	-3	-3	2	2	-1	-1	3	3	-2	-2	1	1	-3	-3	2	2	-1	-1	3	3	-2	-2

**Figure 1.** The arrangement of conductors in a three-phase single-layer machine with  $Z = 24$  slots and  $2p = 4$  poles. The rows of the table stand for, respectively, slot number, and the first layer. Each color and number are associated with a phase.

According to Figure 1, initially, there is one side of a coil, belonging to phase 1 and with a positive current. From Equation (6), the initial argument is 0. Thus, the EMF contributions of the coils of phase 1 in Figure 1 are determined as

$$EMF_{1,1} = 1 \angle \phi_1 = 1 \angle 0^\circ$$

$$EMF_{1,2} = 1 \angle \phi_2 = 1 \angle 30^\circ$$

and so on.

It can be seen from Figure 1 that the coils belonging to the first phase occupy slots 1, 2, 7, 8, 13, 14, 19, and 20. Therefore, Table 1 is filled with the contribution of all side coils of phase 1. The last line of Table 1 is the complex sum of the last-column phasors.

**Table 1.** EMF associated with the first phase in a three-phase single-layer induction motor with  $Z = 24$  slots and  $2p = 4$  poles.

$EMF_{phase+, \phi_k}$	Slots	Current Direction	$\phi_k$ (deg)	Phasor
$EMF_{1,1}$	1	+1	0	$1 \angle 0^\circ$
$EMF_{1,2}$	2	+1	30	$1 \angle 30^\circ$
$EMF_{1,7}$	7	-1	180	$1 \angle 0^\circ$
$EMF_{1,8}$	8	-1	210	$1 \angle 30^\circ$
$EMF_{1,13}$	13	+1	360	$1 \angle 0^\circ$
$EMF_{1,14}$	14	+1	390	$1 \angle 30^\circ$
$EMF_{1,19}$	19	-1	540	$1 \angle 0^\circ$
$EMF_{1,20}$	20	-1	570	$1 \angle 30^\circ$
$EMF_1$	—	—	—	$7.72 \angle 15^\circ$

In a similar way, the total EMF generated by the other phases can be determined. The results are shown in Table 2.

Figure 2 shows the resulting phasor diagram representation for this winding. Red dashed lines are the individual contributions from each coil side, obtained from Table 1. Solid lines are the resulting phasor voltage.

**Table 2.** EMF associated with the winding of a three-phase single-layer induction motor with  $Z = 24$  slots and  $2p = 4$  poles.

$EMF_{phase}$	Phasor
$EMF_1$	$7.72 \angle 15^\circ$
$EMF_2$	$7.72 \angle 135^\circ$
$EMF_3$	$7.72 \angle -105^\circ$

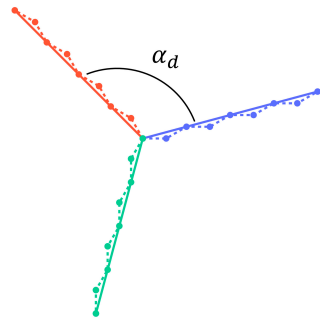


**Figure 2.** The phase diagram for a three-phase single-layer induction motor with  $Z = 24$  slots and  $2p = 4$  poles where each color represents a phase. The dashed lines are the individual phasor voltage from each slot while the solid line is the resultant phasor voltage.  $\alpha_d$  is the angle between the phases.

The displacement angle  $\alpha_d$  for normal or non-reduced systems is determined as shown in Equation (7), and for reduced systems as shown in Equation (8).

$$\alpha_d = \frac{360}{m} \text{ (deg)} \tag{7}$$

$$\alpha_d = \frac{180}{m} \text{ (deg)} \tag{8}$$

Therefore, there is symmetry between the phasors from the diagram of Figure 2 being correctly shifted by  $\alpha_d = \alpha_{ph} = 360/m = 360/3 = 120$  deg from each other, and all phasors have the same magnitude as this is a symmetric winding.

### 2.1.3. Winding Distribution Table

The winding distribution table (WDT) is a method of determining the winding distribution for single and multiphase alternating current (AC) machines described in [30].

The method starts from an empty table containing  $m$  rows and  $n_c$  columns, according to Table 3, where

$$n_c = \frac{Z}{m} \tag{9}$$

**Table 3.** Basic structure of the winding distribution table.

$a_{11}$	$a_{12}$	...	$a_{1n_c}$
$a_{21}$	$a_{22}$	...	$a_{2n_c}$
$\vdots$	$\vdots$	$\ddots$	$\vdots$
$a_{m1}$	$a_{m2}$	...	$a_{mn_c}$

It is assumed that the first element of the table,  $a_{11}$ , corresponds to slot 1. Then, starting from the position of the newly allocated slot, count, from left to right and top to bottom,  $p$  (number of pole pairs) elements and set slot 2. To allocate slot 3, add  $p$  elements to the newly allocated position of slot 2. The procedure continues until all slots have been allocated. If, when adding  $p$  elements, it reaches a position already occupied by another slot, it moves to the adjacent position until an empty position is reached.

To illustrate this method, consider the three-phase single-layer machine with  $Z = 24$  slots and  $2p = 4$  poles and its primitive winding distribution table, according to Table 4.

In fact, the winding distribution table for this machine consists of  $t' = 2$  subsystems and, therefore, two sub-tables, where

$$Z' = \frac{Z}{t'} \tag{10}$$

$$p' = \frac{p}{t'} \tag{11}$$

$$n'_c = \frac{Z'}{t'} \tag{12}$$

**Table 4.** Primitive winding distribution table of a three-phase single-layer machine with  $Z = 24$  slots and  $2p = 4$  poles.

1	13	2	14	3	15	4	16
5	17	6	18	7	19	8	20
9	21	10	22	11	23	12	24

Therefore, the sub-tables have  $Z' = 24/2 = 12$  slots and  $p' = 2/2 = 1$  pole. The first sub-table receives slots from 1 to 12 and contains 1 pair of poles, according to Table 5. The second table, in turn, contains slots 13 to 24, also having 1 pair of poles, according to Table 6.

**Table 5.** Sub-table 1 of winding distribution of a three-phase single-layer machine with  $Z = 24$  slots and  $2p = 4$  poles.

1	2	3	4
5	6	7	8
9	10	11	12

**Table 6.** Sub-table 2 of winding distribution of a three-phase single-layer machine with  $Z = 24$  slots and  $2p = 4$  poles.

13	14	15	16
17	18	19	20
21	22	23	24

For normal (odd number of phases) or non-reduced systems (even number of phases and multiple of 3), after forming the primitive table it is necessary to roll the rows of the “right member” of the table upwards  $\zeta$  times and multiply all elements of “right member” by  $-1$ , where

$$\zeta = \frac{m - 1}{2}, \text{ if } m \text{ is odd.} \tag{13}$$

$$\zeta = \frac{m}{2} - 1, \text{ if } m \text{ is even.} \tag{14}$$

This procedure is demonstrated in Figure 3.

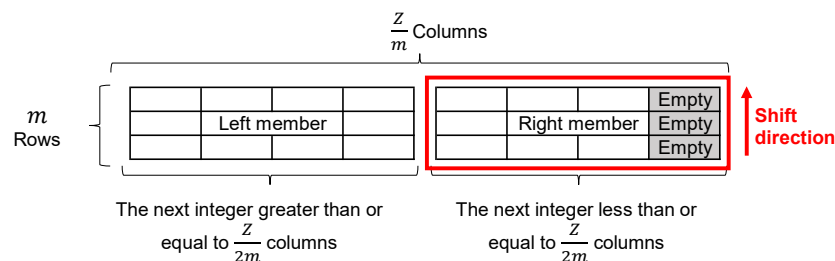


**Figure 3.** Illustration of “right member” shift of the primitive winding distribution tables of normal and non-reduced systems.

If the winding has empty slots, these must be removed from the winding distribution table, excluding the last columns on the right member. In Figure 3, there is an example of a winding that has 3 empty slots, so the last column on the right of the table must be deleted. After removing columns, the “right and left members” of the table must be redistributed.

After scrolling the rows of the “right member”, each row of the table represents the slots occupied by a phase and the direction of current in the conductors, as represented in the Table 7 (table shift of Table 4), where each color is associated with a phase.

**Table 7.** Winding distribution table for a three-phase single-layer machine with  $Z = 24$  slots and  $2p = 4$  poles. Each color is associated with a phase.

1	13	2	14	-7	-19	-8	-20
5	17	6	18	-11	-23	-12	-24
9	21	10	22	-3	-15	-4	-16

If a reduced system is being considered, the winding distribution table is not affected by the vertical shift described above. In these cases, quadrants 1 and 3 of Figure 4 are swapped, and then, the “new right member” of the table is multiplied by  $-1$ .

After this operation, the rows of the primitive table must be reordered in an interleaved way, as shown in Tables 8 and 9.

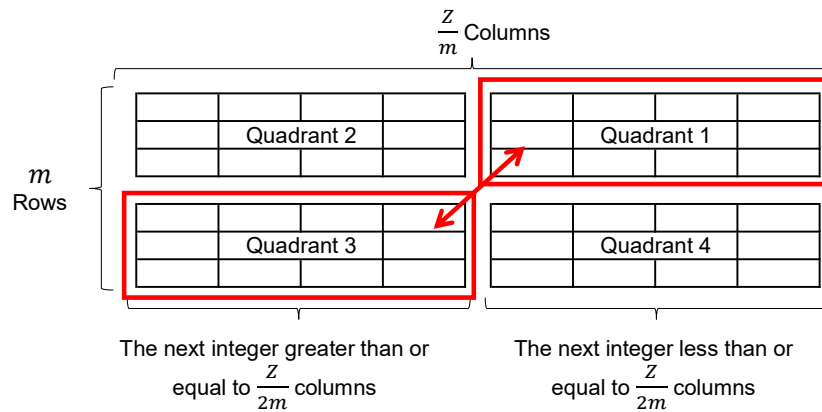


**Figure 4.** Illustration of the swap of quadrants 1 and 3 of primitive winding distribution tables of reduced systems.

**Table 8.** Winding distribution table not yet reordered for reduced systems.

Phases	Col. 1	...	Col. $Z/m$
1	...	...	...
⋮	...	...	...
$\frac{m}{2}$	...	...	...
$\frac{m}{2} + 1$	...	...	...
⋮	...	...	...
$m$	...	...	...

**Table 9.** Reordered winding distribution table for reduced systems.

Phases	Col. 1	...	Col. $Z/m$
1	...	...	...
$\frac{m}{2} + 1$	...	...	...
2	...	...	...
$\frac{m}{2} + 2$	...	...	...
⋮	...	...	...
$\frac{m}{2}$	...	...	...
$m$	...	...	...

Reduced systems whose number of phases are not powers of 2 are composed of  $m_g$  subgroups of systems with  $m_u$  phases each, where

$$m_u = mpf(m) \tag{15}$$

is the maximum prime fact of  $m$ , and

$$m_g = \frac{m}{m_u} \tag{16}$$

Therefore, a system that has 12 phases can be decomposed into  $m_g = 4$  subgroups of systems with  $m_u = 3$  phases each. The even phases of each subgroup must be multiplied by  $-1$  to obtain radial symmetry and avoid using a neutral line.

If the machine has two layers, the winding distribution table originally computed for a single layer must be concatenated with a copy of it, but shifted by the coil pitch  $y$  and multiplied by  $-1$ .

To elucidate the WDT computation for reduced systems, consider a machine with  $m = 4$  phases,  $Z = 32$  slots,  $2p = 4$  poles, double layer, and coil pitch of  $y = 3$  slots. The primitive WDT computed for this machine is shown in Table 10. In Table 11, the WDT of the first layer is shown after swapping quadrants 1 and 4 and multiplying the “right member” by  $-1$ . In Table 12, there is the WDT for the first layer after row reordering, as described by Table 9. Table 13 shows the second-layer WDT (copy of the first-layer table, shifted by the coil pitch  $y = 3$  slots and multiplied by  $-1$ ). Finally, in Figure 5 the arrangement of conductors for this machine is shown.

**Table 10.** Primitive WDT for a machine with  $m = 4$  phases,  $Z = 32$  slots, double layer, and coil pitch of  $y = 3$  slots.

1	17	2	18	3	19	4	20
5	21	6	22	7	23	8	24
9	25	10	26	11	27	12	28
13	29	14	30	15	31	16	32

**Table 11.** First-layer WDT after swapping quadrants 1 and 4 and multiplying the “right member” by  $-1$  for a machine with  $m = 4$  phases,  $Z = 32$  slots, double layer, and coil pitch of  $y = 3$  slots.

1	17	2	18	-9	-25	-10	-26
5	21	6	22	-13	-29	-14	-30
3	19	4	20	-11	-27	-12	-28
7	23	8	24	-15	-31	-16	-32

**Table 12.** The first-layer WDT after row reordering for a machine with  $m = 4$  phases,  $Z = 32$  slots, double layer, and coil pitch of  $y = 3$  slots.

1	17	2	18	-9	-25	-10	-26
3	19	4	20	-11	-27	-12	-28
5	21	6	22	-13	-29	-14	-30
7	23	8	24	-15	-31	-16	-32

**Table 13.** The second-layer WDT for a machine with  $m = 4$  phases,  $Z = 32$  slots, double layer, and coil pitch of  $y = 3$  slots.

-4	-20	-5	-21	12	28	13	29
-6	-22	-7	-23	14	30	15	31
-8	-24	-9	-25	16	32	17	1
-10	-26	-11	-27	18	2	19	3

1	2	3	4	5	6	7	8	9	10	11	12	13	14	15	16	17	18	19	20	21	22	23	24	25	26	27	28	29	30	31	32
1	1	2	2	3	3	4	4	-1	-1	-2	-2	-3	-3	-4	-4	1	1	2	2	3	3	4	4	-1	-1	-2	-2	-3	-3	-4	-4
3	4	4	-1	-1	-2	-2	-3	-3	-4	-4	1	1	2	2	3	3	4	4	-1	-1	-2	-2	-3	-3	-4	-4	1	1	2	2	3

**Figure 5.** The arrangement of conductors in a machine with  $m = 4$  phases,  $Z = 32$  slots,  $2p = 4$  poles, double layer, and coil pitch of  $y = 3$  slots. The rows of the table stand for, respectively, the slot number, the first layer, and the second layer. Each color and number are associated with a phase.

The vertical shifting or quadrant swapping and reordering operations made with the primitive WDTs are necessary to achieve radially symmetrical windings, avoiding the use of a neutral line in reduced systems. Note that the WDT computed for the machine with  $m = 4$  phases,  $Z = 32$  slots, double layer, and coil pitch of  $y = 3$  slots results in a symmetric magnetomotive force (MMF) curve along the slots, as shown in Figure 6.

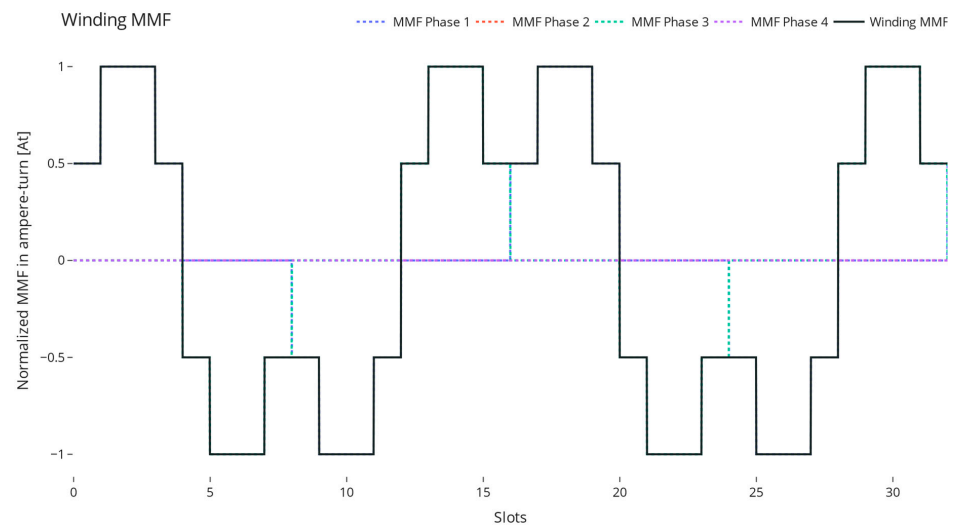


**Figure 6.** The MMF curve of a machine with  $m = 4$  phases,  $Z = 32$  slots, double layer, and coil pitch of  $y = 3$ .

### 2.2. Total Harmonic Distortion of the MMF of the Winding

The air gap magnetomotive force (MMF) is the effect of the electric current flowing through conductors. The MMF waveform depends mainly on the coil span and distribution, and air gap geometry.

#### 2.2.1. Magnetomotive Force (MMF) of a Winding

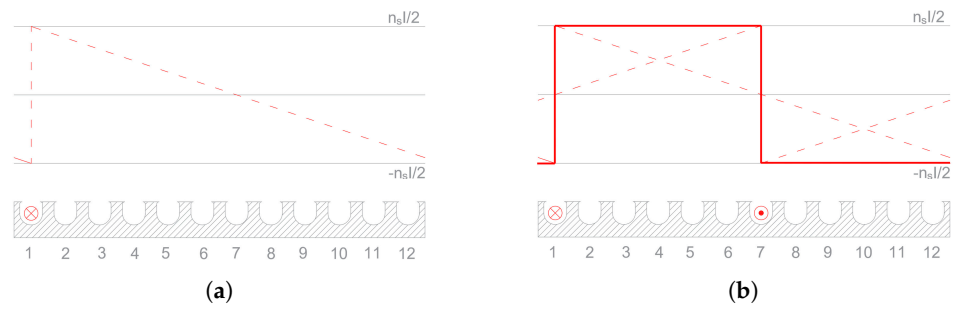
The waveform of the MMF generated in the air gap of a machine by a conductor carrying current can be satisfactorily approximated by a “sawtooth” wave [31,32].

Figure 7a shows the MMF generated by  $n_s$ -phase conductors of slot 1 of a single-layer machine winding with  $Z = 12$  slots and  $2p = 2$  poles. The instantaneous conductor current  $i$  is assumed as constant and directed axially.

The returning conductor of the coil with it is corresponding current and respective MMF is illustrated in Figure 7b. Conductors in slots 1 and 7 form a coil belonging to phase 1 and, together, generate a rectangular MMF, corresponding to the sum of the individual contributions of the conductors belonging to each slot [32].

This methodology permits the total MMF of the entire winding to be obtained. For the 12 slots example, the resulting three-phase MMF obtained is as shown in Figure 8.

In this work, the quality of the MMF wave generated by the proposed winding is analyzed. Therefore, as shown in Figure 9, the amplitude of the MMF wave is normalized.



**Figure 7.** Composition of the MMF of phase 1 of a three-phase single-layer machine with  $Z = 12$  slots and  $2p = 2$  poles. (a) MMF produced by  $n_s$  conductors of phase 1 belonging to slot 1. (b) MMF produced by a 1-phase coil placed in slots 1 and 7.

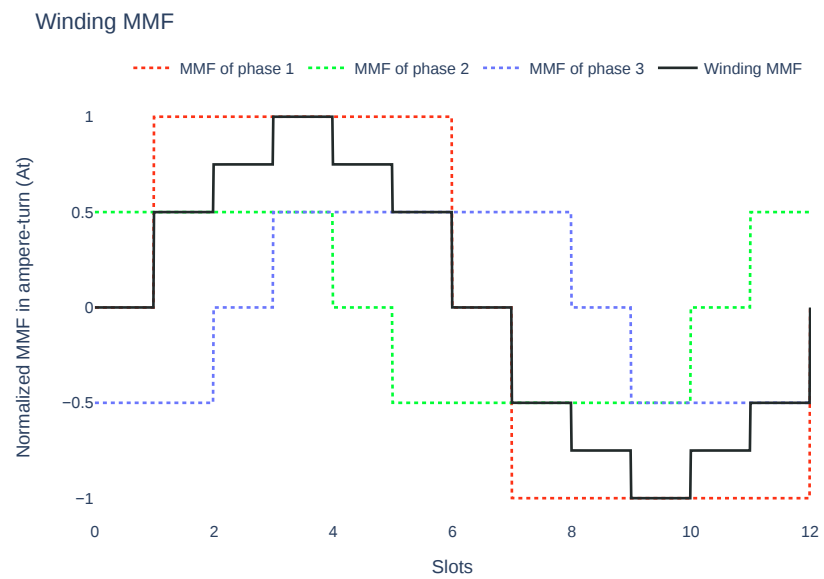


**Figure 8.** Total MMF curve composition of a three-phase single-layer machine with  $Z = 12$  slots and  $2p = 2$  poles.

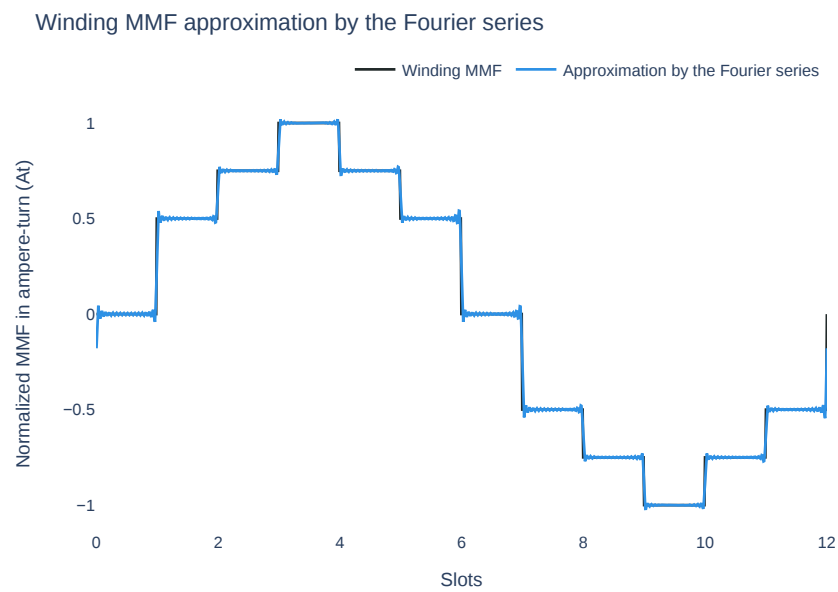


**Figure 9.** Fourier series approximation of the MMF curve of a three-phase single-layer machine with  $Z = 12$  slots and  $2p = 2$  poles.

### 2.2.2. Total Harmonic Distortion (THD)

Once the MMF wave is obtained, its decomposition by the Fourier series can be calculated by Equation (17).

$$F(\theta) = \sum_{n=1}^{\infty} a_n \cos\left(n \frac{2\pi}{\tau_0} \theta\right) + b_n \sin\left(n \frac{2\pi}{\tau_0} \theta\right) \quad (17)$$

where

$$a_n = \frac{2}{\tau_0} \int_0^{\tau_0} F(\theta) \cos\left(n \frac{2\pi}{\tau_0} \theta\right) d\theta \quad (18)$$

$$b_n = \frac{2}{\tau_0} \int_0^{\tau_0} F(\theta) \sin\left(n \frac{2\pi}{\tau_0} \theta\right) d\theta \quad (19)$$

In Equations (17)–(19),  $\tau_0$  is the period of the fundamental wave in radians,  $n$  is the harmonic order, and  $\theta$  is the angular position, also in radians.

In Figure 9, the Fourier series approximation of the MMF curve of a three-phase machine with  $Z = 12$  slots and  $2p = 2$  poles and a single layer is represented, as postulated in Equation (17), with a maximum harmonic limit of  $n = 200$ .

The THD is an important quality parameter of the generated MMF, since it numerically quantifies the influence of the harmonics present in the MMF. The THD is determined as shown in Equation (20).

$$\text{THD} = \frac{1}{C_f} \sqrt{\sum_{n=2}^{\infty} C_n^2} \quad (20)$$

where

$$C_n = \sqrt{a_n^2 + b_n^2} \quad (21)$$

$$C_f = \sqrt{a_1^2 + b_1^2} \quad (22)$$

The closer the THD is to zero, the lower the harmonic content present and, therefore, the less distortion there will be in the MMF wave of the proposed winding.

### 2.3. End-Winding Leakage Inductance

Within rotating machines, a portion of the magnetic flux deviates from the primary path responsible for electromechanical energy conversion. These leakage fluxes, as explored by Jokinen in [28], induce a heightened skin effect within the stator slot conductors, consequently elevating stator copper losses. Furthermore, Lipo, in [8], established a fundamental link between leakage inductance and crucial machine characteristics, including starting torque, maximum torque, rotor currents, and stator currents. This inherent connection underscores the significant impact of leakage inductance on the performance, applicability, and material selection for both motors and generators. Therefore, optimizing these interrelated effects becomes paramount from both economic and energy efficiency perspectives.

The end-winding dispersion flux, illustrated by Figure 10a from the side cutaway of an electrical machine with stator windings, corresponds to flux lines outside the magnetic package and an air gap coming from the end or turns of the coils.

In [33], there is an analytical and empirical study of the leakage inductance from windings with diamond-shaped coils, as shown in Figure 10b representing two adjacent coil ends of an electrical machine stator.

The end-winding leakage inductance per phase  $L_{ew}$  is determined according to Equation (23).

$$L_{ew} = \frac{9,6}{Z} \mu_0 m k_{p1}^2 k_{d1}^2 N_s^2 \left( l_{e2} + \frac{l_{e1}}{2} \right) \quad (23)$$

where

$$l_{e1} = \frac{y \tau_{p(ave)} (b_c + t_e)}{2 \sqrt{\tau_{s(ave)}^2 - (b_c + t_e)^2}} \quad (24)$$

$$b_c + t_e = \text{sen}(\sigma)\tau_s \quad (25)$$

where  $b_c$  corresponds to the slot depth,  $t_e$  the slot tooth width, and  $\tau_{s(\text{bird})}$  the slot width.

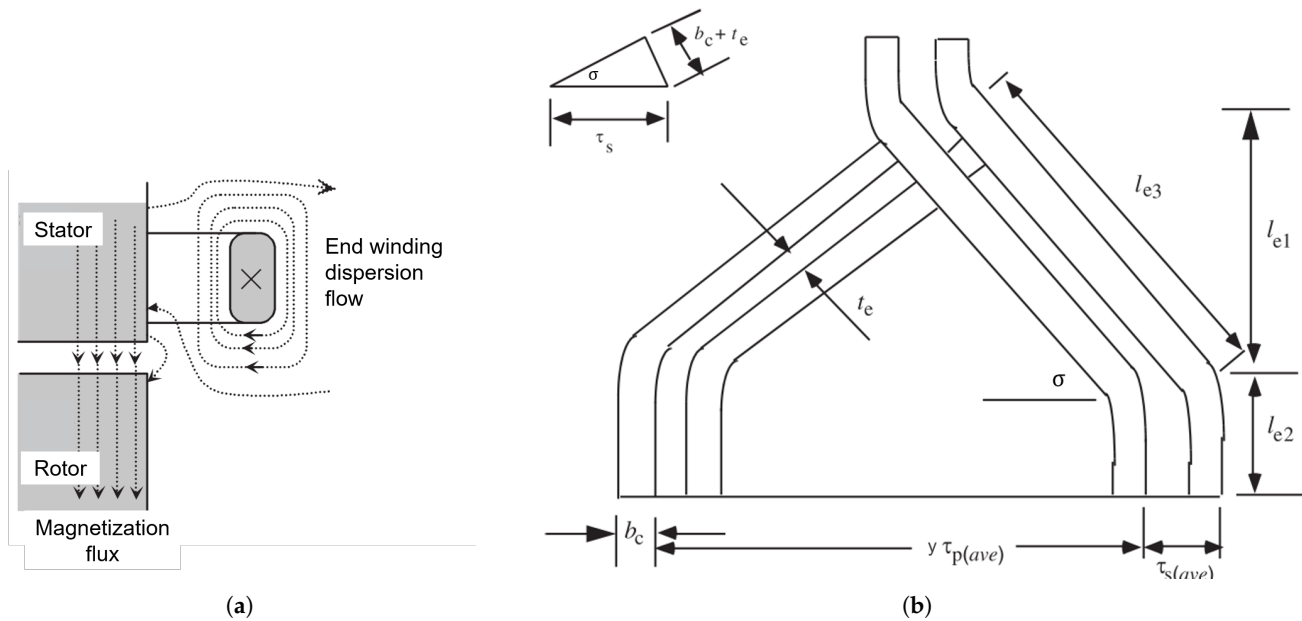


**Figure 10.** Illustration of end-winding dispersion flux. (a) The end-winding dispersion flux in side cutaway view. (b) Two adjacent diamond coil ends of an electrical machine stator.

Also,  $\mu_0$  is the vacuum magnetic permeability constant;  $k_{p1}$  and  $k_{d1}$  are, respectively, the pitch factor and the distribution factor, both for the fundamental frequency; and  $l_{e2}$  and  $l_{e1}$  are constructive geometric parameters of the winding, as shown in Figure 10b.  $N_s$  is the number of turns connected in series per phase,  $m$  is the number of phases in the system, and  $Z$  is the number of slots in the machine.

This work considers lap and wavy windings with geometrically symmetric coils, so  $\tau_s = \tau_{s(\text{ave})}$  and  $y\tau_{s(\text{ave})} = y\tau_{p(\text{ave})}$ . The constructive parameters of the coils, for all the studied machines, were taken as being  $N_s = 1$  turn,  $l_{e2} = 15$  mm,  $\tau_s = 10$  mm,  $\sigma = 30^\circ$ , and therefore,  $b_c + t_e = 5$  mm.

#### 2.4. Multi-Objective Particle Swarm Optimization (MOPSO)

Among the numerous existing implementations of metaheuristics, this work uses particle swarm optimization (PSO) and multi-objective problem solving concepts using Pareto frontiers [34,35] to find optimized proposals for electrical windings that simultaneously produce MMF curves with lower THD and lower end-winding leakage inductance.

In the algorithm, each particle (possible solution) has a position and a velocity described by Equations (26) and (27).

$$\vec{p}_{i,t}(\vec{x}) = (x_{1i}, x_{2i}, x_{3i}, \dots, x_{ji}) \quad (26)$$

$$\vec{v}_{i,t}(\vec{x}) = W\vec{v}_{i,t-1}(\vec{x}) + c_1r_1[\vec{p}_i^{\text{best}} - \vec{p}_{i,t}(\vec{x})] + c_2r_2[\vec{p}_{g\text{best}} - \vec{p}_{i,t}(\vec{x})] \quad (27)$$

where  $\vec{p}_{i,t}(\vec{x})$  and  $\vec{v}_{i,t}(\vec{x})$  are, respectively, the position and velocity of particle  $i$  at iteration  $t$ ; and  $\vec{x}$  is the vector of positions for each  $j$  dimension (machine parameter).  $\vec{p}_i^{\text{best}}$  is the best position found by particle  $i$  in its trajectory and  $\vec{p}_{g\text{best}}$  is the best position found by the swarm so far. The  $r_1$  and  $r_2$  coefficients are random numbers between 0 and 1 used to introduce uncertainty and avoid local optima and premature convergence.  $c_1$  and  $c_2$  are the influence factors for the individual and collective search, respectively.  $W$  is the inertia coefficient that tries to hold the particle in its trajectory.

For each iteration, the new positions of the particles are computed by Equation (28).

$$\vec{p}_{i,t+1}(\vec{x}) = \vec{p}_{i,t}(\vec{x}) + \vec{v}_{i,t}(\vec{x}) \quad (28)$$

As this is a multi-objective problem, the Pareto frontier and the density criteria are used to classify the solutions and  $\vec{p}_{g_{best}}$ , respectively, as described below.

Consider a multi-objective problem described by Equations (29), where  $\vec{y}(\vec{x})$  is the set of fitness functions  $f_1(\vec{x}), f_2(\vec{x}), \dots, f_k(\vec{x})$  to be optimized and Equations (30) and (31) are constrain functions.

$$\min[\vec{y}(\vec{x})] := [f_1(\vec{x}), f_2(\vec{x}), \dots, f_k(\vec{x})] \quad (29)$$

$$g_l(\vec{x}) \leq 0, \quad l = 1, 2, \dots, m \quad (30)$$

$$h_j(\vec{x}) = 0, \quad j = 1, 2, \dots, p \quad (31)$$

The Pareto frontier is defined by the best solutions that are not fully dominated by any other. For illustration, consider the bi-objective minimization problem shown in Figure 11a, where the green points are the solutions that form the Pareto frontier. After some iterations of PSO, it is expected that the Pareto front is well distributed and as close to the minimum as possible, without trespassing the constraints  $g_l(\vec{x})$  and  $h_j(\vec{x})$ , as shown in Figure 11b.

There are some approaches to determine the  $\vec{p}_{g_{best}}$ , such as the niche count, the  $\epsilon$ -dominance, and the density criterion  $\delta$ . The last one is implemented in this work and described in Equation (32).

$$\delta_i = \frac{k}{\sum_{j=1}^k d_{ij}} \quad (32)$$

where  $k$  is the number of neighbors considered for computation and  $d_{ij}$  is the Euclidean distance between solutions  $i$  and  $j$ , as shown in Figure 11c.

For each iteration, the solution with the lowest density is selected as  $\vec{p}_{g_{best}}$ . This uniformly populates the Pareto frontier.

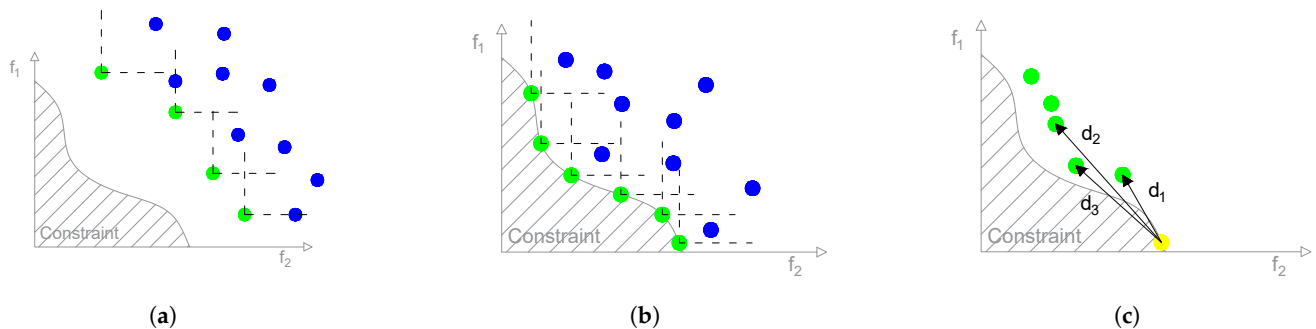


**Figure 11.** The evolution of the Pareto frontier during a bi-objective optimization problem solving. The green points stand for non-dominated solutions, the blue points are the dominated solutions, and the yellow point is the solution for which the density is being calculated. The hatched area is the area delimited by constraints. (a) The beginning of optimization. The Pareto frontier is far from the optimized solution set. (b) The expected optimization results. The Pareto frontier is at the limit of the restrictions to achieve the set of optimized solutions. (c) The density criterion computation for the yellow solution.

The cases to be solved in this work are formulated by first restricting the acceptable parameter ranges (dimensions):

- $m$ , the number of phases;
- $Z$ , the number of slots;
- $p$ , the number of pole pairs;
- $n_{lay}$ , the number of layers;
- $y$ , the coil pitch.

The algorithm seeks  $\min(\text{THD}, L_{ew})$ . For each proposed winding (particle), the feasibility of the winding is verified. For each valid winding, MMF, THD, and  $L_{ew}$  are computed. The flow diagram of the algorithm is the same as the classic MOPSO, as shown in Figure 12.

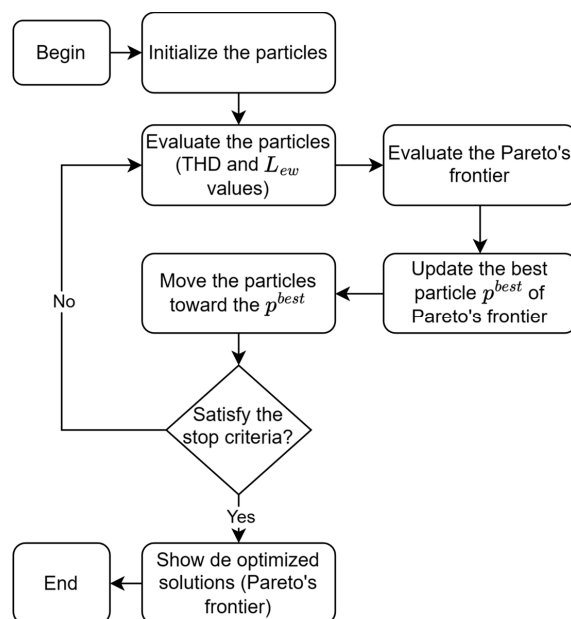


**Figure 12.** Flow diagram of the methodology applied to optimize the windings.

The methodology used to verify the accuracy of the algorithm is described in Section 3.1.

### 3. Results

#### 3.1. Validation Tests

To validate the accuracy and robustness of the application, the algorithm was submitted to two different validation scenarios, according to Table 14. For each scenario, all possible solutions were computed (without optimization strategies) to check their solution sets in an integral way by identifying local and global optima in order to compare them with the solutions that were found by MOPSO. The last column of Table 14 represents the number of possible windings within the search space defined by changing the constructive parameters.

**Table 14.** Validating solution scenarios by the application.

Scenario	$m$	$Z$	$p$	$n_{lay}$	$y$	Possibilities
1	3	3–90	1–3	2	1–4	1056
2	6	120–180	3–5	1–2	1–6	1281

Based on the validation tests, it was possible to correctly choose the inertia coefficient  $W = 0.3$  and the individual influence ( $c_1 = 0.5$ ) and collective influence ( $c_2 = 1$ ) coefficients. The swarm size is 5% of the total possibilities for the search field defined.

For better graphic representation, all the figures presented in this section have the ordinate  $L_{ew}$ , in henry (H) and on a logarithmic scale of base 10, while the abscissas, THD, are on an arithmetic scale.

##### 3.1.1. Validation Scenario 1

According to Table 14, the search space belonging to validation scenario 1 contains normal systems (odd number of phases) and is restricted to double-layer windings.

In Figure 13, the ideal Pareto frontier is represented in yellow circles, and the Pareto frontier computed by MOPSO is shown in black diamonds. For this scenario, the solu-

tions obtained by the algorithm reached an accuracy of 94%, finding 16 of the 17 global optimal solutions.

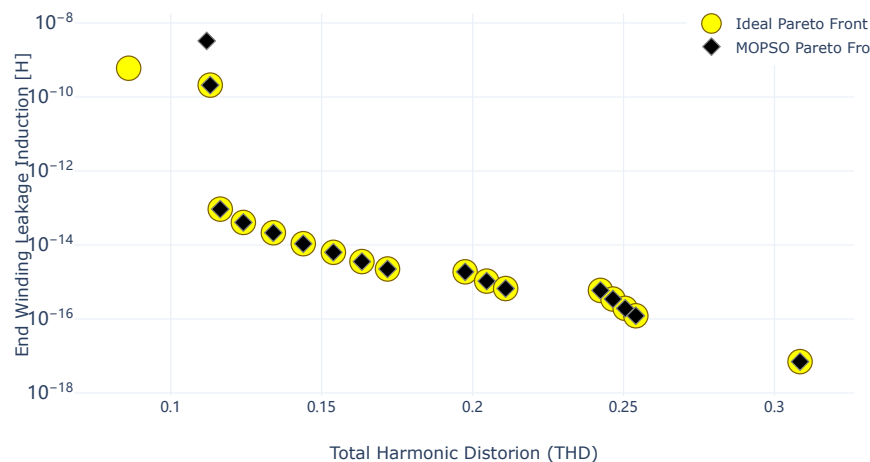


Figure 13. Ideal Pareto frontier and MOPSO for validation scenario 1.

### 3.1.2. Validation Scenario 2

The search space for validation scenario 2, according to Table 14, refers to non-reduced systems (even number of phases and multiple of 3) comprising single- and double-layer windings.

In Figure 14, the ideal Pareto frontier is represented in yellow circles, and the Pareto frontier computed by MOPSO is shown in black diamonds. The performance of the algorithm for this scenario was 93%, finding 14 out of 15 global optimal solutions.

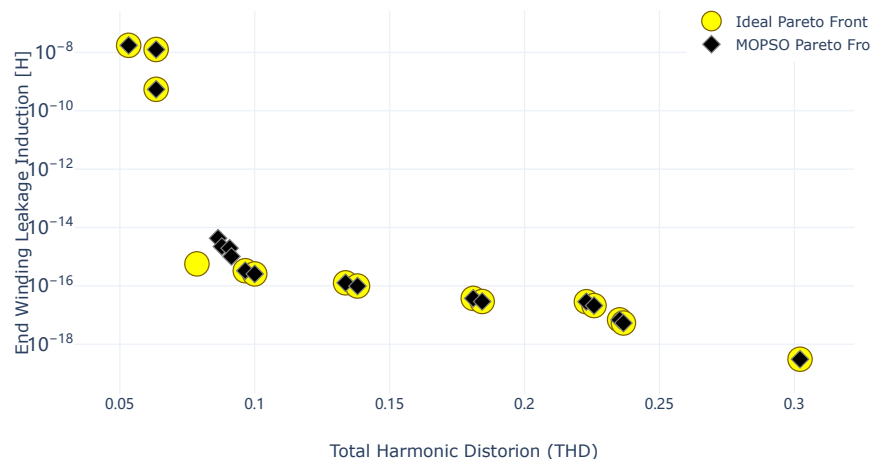


Figure 14. Ideal Pareto frontier and MOPSO for validation scenario 2.

### 3.2. Application

Once the accuracy of the optimization algorithm has been proven, obtaining in all cases an accuracy greater than 90%, the resolution methodology can be extrapolated to cases with vast search spaces and complex configurations; see Table 15.

Table 15. Application scenarios.

Scenario	$m$	$Z$	$p$	$n_{lay}$	$y$	Possibilities
1	3	3–300	1–6	1–2	1–4	8940
2	5–7	70–210	1–6	1–2	1–4	12,690
3	9–12	90–250	1–5	1–2	1–8	28,980

For the application cases described in this section, to which the algorithm was submitted, the Pareto frontier is computed by MOPSO and there is no comparison between the ideal solution (global optimum) since there is a high computational effort in the integral exploration of the search spaces, making this type of solution unfeasible.

### 3.2.1. Application Scenario 1

According to Table 15, the search space belonging to application scenario 1 refers to single- and double-layer three-phase systems.

In Figure 15, the Pareto frontier computed by MOPSO is shown in black diamonds.

The results found, which add up to 36 different windings, demonstrate a satisfactory distribution of solutions on the Pareto frontier, indicating that the solution is not prematurely biased.

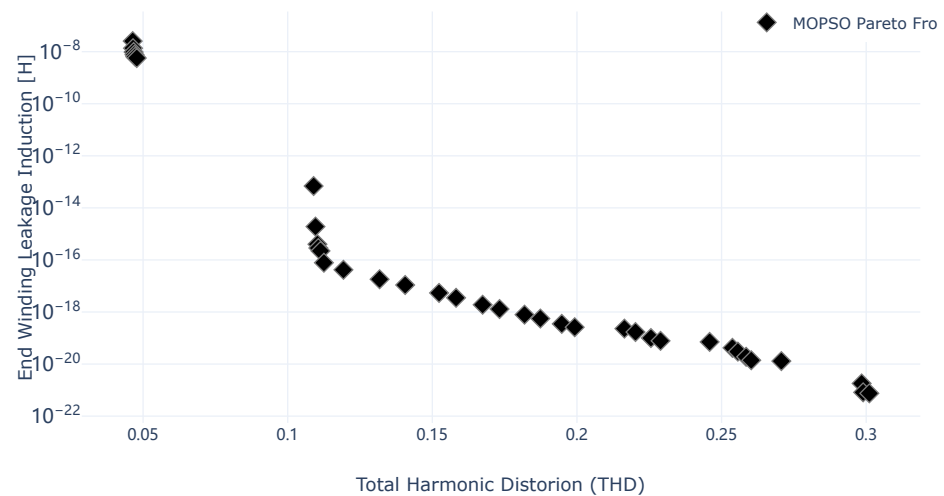


**Figure 15.** Pareto frontier computed by MOPSO for application scenario 1.

### 3.2.2. Application Scenario 2

The search space belonging to application scenario 2, shown in Table 15, contains normal and non-reduced systems covering single- and double-layer windings.

Again, in Figure 16, the Pareto frontier computed by MOPSO is shown in black diamonds.

A satisfactory distribution of the solutions on the Pareto frontier is observed, computing values in both THD and  $L_{ew}$  limits.

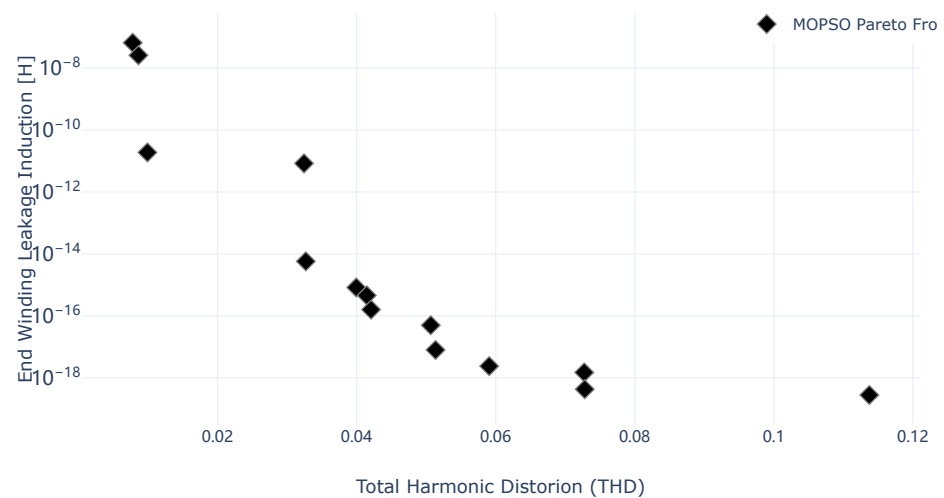


**Figure 16.** Pareto frontier computed by MOPSO for application scenario 2.

### 3.2.3. Application Scenario 3

As in the previous cases, application scenario 3 and its search space are listed in Table 15, composed of normal and non-reduced systems that cover single- and double-layer windings.

In Figure 17, the Pareto frontier computed by MOPSO is shown in black diamonds.

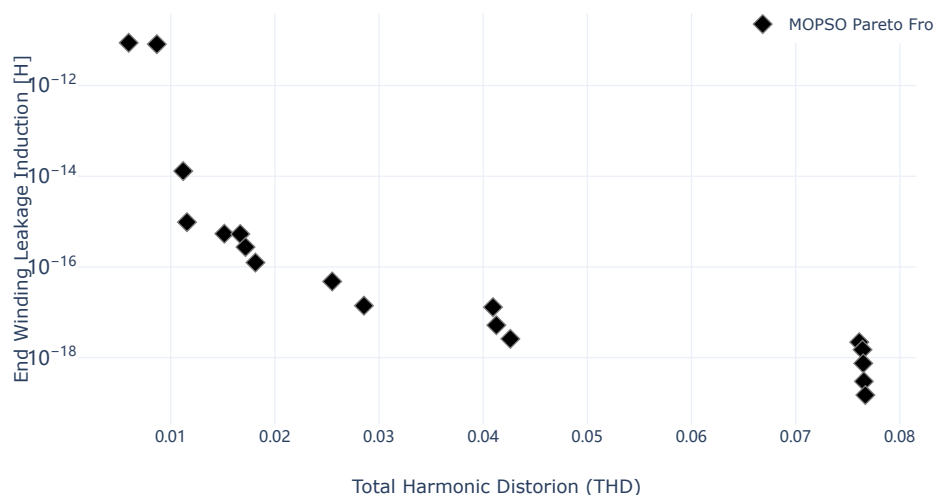


Figure 17. Pareto frontier computed by MOPSO for application scenario 3.

## 4. Discussion

While a comprehensive comparison with existing methods remains challenging due to the limited application of metaheuristics to poly-phase machine optimization, the MOPSO approach demonstrates several advantages. Unlike analytical methods, which can struggle with intricate machine designs, MOPSO efficiently navigates large search spaces defined by numerous winding parameters. This capability allows the algorithm to identify near-optimal solutions for complex motor configurations. However, as an iterative algorithm, MOPSO may require significant computational time to achieve absolute optimality, depending on the problem's complexity.

The effectiveness of the MOPSO approach is further validated by its ability to perform bi-objective minimization optimization of the THD of the MMF curve and the end-winding leakage inductance with approximately 20 times less computational effort compared to an exhaustive search of the solution space. Validation tests yielded accuracy exceeding 90%, demonstrating the algorithm's robustness in finding optimized solutions. Consequently, MOPSO proves to be a valuable tool for tackling complex and extensive search spaces encountered in electrical machine design.

Beyond optimization, the application extends its functionality to user-friendly visualization. For any electrical machine with feasible windings, the application can generate graphical representations of the winding diagram by the WDT and the phasor diagram. Additionally, for symmetrical windings, the application computes the MMF curve by phase and its corresponding Fourier series approximation. This comprehensive visualization suite effectively communicates the results to the user, providing valuable insights into the optimized winding design.

## 5. Conclusions

In conclusion, this paper proposes a MOPSO approach for optimizing winding design in poly-phase machines. MOPSO effectively tackles complex winding configurations, achieving high accuracy in validation tests, and offers a powerful tool for real-world electrical machine design. By integrating the presented methodology into a comprehensive design framework, engineers can optimize motor windings for specific applications, potentially reducing energy losses by THD minimization and improving motor performance

by end-winding leakage inductance reduction. This can lead to the development of more efficient and reliable electrical machines for various industrial applications.

Future research can explore techniques to accelerate convergence or combine MOPSO with local optimization methods for fine-tuning. Additionally, a broader comparison with existing methods would be valuable once more studies utilizing metaheuristics for poly-phase machine optimization become available.

**Author Contributions:** Conceptualization, B.P.A. and G.T.P.; formal analysis, F.S.M.; investigation, F.S.M., B.P.A. and G.T.P.; methodology, B.P.A. and G.T.P.; project administration, F.S.M.; supervision, B.P.A. and G.T.P.; validation, F.S.M.; writing—original draft, F.S.M.; writing—review and editing, F.S.M., B.P.A. and G.T.P. All authors have read and agreed to the published version of the manuscript.

**Funding:** This research received no external funding.

**Data Availability Statement:** The original contributions presented in the study are included in the article, further inquiries can be directed to the corresponding author.

**Conflicts of Interest:** The authors declare no conflicts of interest.

### Abbreviations

The following abbreviations are used in this manuscript:

AC	Alternating current
BESO	Bi-directional evolutionary structural optimization
EMF	Electromotive force
MMF	Magnetomotive force
MOPSO	Multi-objective particle swarm optimization
SIMP	Solid-isotropic material with penalization
THD	Total harmonic distortion
WDT	Winding distribution table

### References

- Jardot, R.; Krebs, G.; Lahlou, A.; Roy, F.; Marchand, C. Calculation of Losses in a Motor Fed by a Conventional Inverter and a Battery Distributed Inverter. *Energies* **2023**, *16*, 7993. [\[CrossRef\]](#)
- Brkovic, B.; Jecmenica, M. Calculation of Rotor Harmonic Losses in Multiphase Induction Machines. *Machines* **2022**, *10*, 401. [\[CrossRef\]](#)
- Roshandel, E.; Mahmoudi, A.; Kahourzade, S.; Yazdani, A.; Shafiullah, G. Losses in Efficiency Maps of Electric Vehicles: An Overview. *Energies* **2021**, *14*, 7805. [\[CrossRef\]](#)
- Franco, A.L.C. Otimização Aplicada ao Projeto de Enrolamentos de máquinas CA. Ph.D. Thesis, UFG, Goiânia, Brazil, 2015.
- Sui, Y.; Zheng, P.; Wu, F.; Yu, B.; Wang, P.; Zhang, J. Research on a 20-Slot/22-Pole Five-Phase Fault-Tolerant PMSM Used for Four-Wheel-Drive Electric Vehicles. *Energies* **2014**, *7*, 1265–1287. [\[CrossRef\]](#)
- Tang, N.; Brown, I.P. Family Phenomenon in Electric Machine Winding MMF Space Harmonics: Attribution and Applications. *IEEE Trans. Magn.* **2019**, *55*, 1–10. [\[CrossRef\]](#)
- Chen, X.; Wang, J. Magnetomotive force harmonic reduction techniques for fractional-slot non-overlapping winding configurations in permanent-magnet synchronous machines. *Chin. J. Electr. Eng.* **2017**, *3*, 102–113. [\[CrossRef\]](#)
- Lipo, T.A. *Introduction to AC Machine Design*; John Wiley & Sons: Hoboken, NJ, USA, 2017.
- Khlifi, M.A. Advances and Steady-State Development of Dual Stator-Winding Induction Machine. *IETE J. Res.* **2022**, *68*, 2934–2940. [\[CrossRef\]](#)
- Wang, Y.; Yang, J.; Deng, R.; Yang, G. Parameters estimation for multiphase induction machine with concentrated windings through finite element method. *IET Electr. Power Appl.* **2020**, *14*, 1807–1817. [\[CrossRef\]](#)
- Nishanth, F.; Wang, B. Topology Optimization of Electric Machines: A Review. In Proceedings of the 2022 IEEE Energy Conversion Congress and Exposition (ECCE), Detroit, MI, USA, 9–13 October 2022; pp. 1–8. [\[CrossRef\]](#)
- Sato, T.; Watanabe, K.; Igarashi, H. Multimaterial Topology Optimization of Electric Machines Based on Normalized Gaussian Network. *IEEE Trans. Magn.* **2015**, *51*, 1–4. [\[CrossRef\]](#)
- Otomo, Y.; Igarashi, H. Topology Optimization Using Gabor Filter: Application to Synchronous Reluctance Motor. *IEEE Trans. Magn.* **2021**, *57*, 1–4. [\[CrossRef\]](#)
- Watanabe, K.; Suga, T.; Kitabatake, S. Topology Optimization Based on the ON/OFF Method for Synchronous Motor. *IEEE Trans. Magn.* **2018**, *54*, 1–4. [\[CrossRef\]](#)
- Garibaldi, M.; Gerada, C.; Ashcroft, I.; Hague, R. Free-Form Design of Electrical Machine Rotor Cores for Production Using Additive Manufacturing. *J. Mech. Des.* **2019**, *141*, 071401. [\[CrossRef\]](#)

16. Huang, X.; Xie, Y.M. A further review of ESO type methods for topology optimization. *Struct. Multidiscip. Optim.* **2010**, *41*, 671–683. [[CrossRef](#)]
17. Zuo, Z.; Xie, Y.; Huang, X. Combining genetic algorithms with BESO for topology optimization. *Struct. Multidiscip. Optim.* **2009**, *38*, 511–523. [[CrossRef](#)]
18. Guo, F.; Brown, I.P. Simultaneous magnetic and structural topology optimization of synchronous reluctance machine rotors. *IEEE Trans. Magn.* **2020**, *56*, 1–12. [[CrossRef](#)]
19. Tcherniak, D. Topology optimization of resonating structures using SIMP method. *Int. J. Numer. Methods Eng.* **2002**, *54*, 1605–1622. [[CrossRef](#)]
20. Wang, M.Y.; Wang, X.; Guo, D. A level set method for structural topology optimization. *Comput. Methods Appl. Mech. Eng.* **2003**, *192*, 227–246. [[CrossRef](#)]
21. Ren, X.; Thabuis, A.; Belahcen, A.; Perriard, Y. Topology optimization for coils of electric machine with level-set method. In Proceedings of the 2019 22nd International Conference on Electrical Machines and Systems (ICEMS), Harbin, China, 11–14 August 2019; IEEE: Piscataway, NJ, USA, 2019; pp. 1–4. [[CrossRef](#)]
22. Lee, J.; Wang, S. Topological shape optimization of permanent magnet in voice coil motor using level set method. *IEEE Trans. Magn.* **2012**, *48*, 931–934. [[CrossRef](#)]
23. Hadžiselimović, M.; Marčič, T.; Štumberger, B.; Zagradišnik, I. Winding type influence on efficiency of an induction motor. *Prz. Elektrotech.* **2011**, *87*, 61–64.
24. Silva, R.C.P.; Rahman, T.; Mohammadi, M.H.; Lowther, D.A. Multiple Operating Points Based Optimization: Application to Fractional Slot Concentrated Winding Electric Motors. *IEEE Trans. Ind. Electron.* **2018**, *65*, 1719–1727. [[CrossRef](#)]
25. Marault, J.; Gillon, F.; Hecquet, M.; Tounzi, A. Optimization of the MMF spatial harmonic content to design electrical machine winding. *Int. J. Appl. Electromagn. Mech.* **2020**, *64*, S99–S114. [[CrossRef](#)]
26. Bekka, N.; Zaïm, M.E.; Bernard, N.; Trichet, D. Optimization of the MMF function of fractional slot concentrated windings. In Proceedings of the 2014 International Conference on Electrical Machines (ICEM), Berlin, Germany, 2–5 September 2014; pp. 616–622. [[CrossRef](#)]
27. Schmitz, N.L.; Novotny, D.W. *Introductory Electromechanics*; Ronald Press: New York, NY, USA, 1965.
28. Jokinen, T.; Hrabovcova, V.; Pyrhonen, J. *Design of Rotating Electrical Machines*; John Wiley & Sons: Hoboken, NJ, USA, 2013.
29. Smolensky, A.I. *Electrical Machines*; Mir: Moscow, Russia, 1983.
30. Caruso, M.; Di Tommaso, A.O.; Marignetti, F.; Miceli, R.; Ricco Galluzzo, G. A General Mathematical Formulation for Winding Layout Arrangement of Electrical Machines. *Energies* **2018**, *11*, 446. [[CrossRef](#)]
31. Hague, B. The mathematical treatment of the magnetomotive force of armature windings. *J. Inst. Electr. Eng.* **1917**, *55*, 489–514. [[CrossRef](#)]
32. Hague, B. *The Principles of Electromagnetism Applied to Electrical Machines: (Formerly Titled: Electromagnetic Problems in Electrical Engineering)*; Dover Publications: Mineola, NY, USA, 1962; Volume 246.
33. Liwshitz-Garik, M. *Electric Machinery*; Van Nostrand: Washington, DC, USA, 1946; Volume 2.
34. Reyes-Sierra, M.; Coello, C.C. Multi-objective particle swarm optimizers: A survey of the state-of-the-art. *Int. J. Comput. Intell. Res.* **2006**, *2*, 287–308. [[CrossRef](#)]
35. Brownlee, J. *Clever Algorithms: Nature-Inspired Programming Recipes*; Jason Brownlee: Austin, TX, USA, 2011.

**Disclaimer/Publisher’s Note:** The statements, opinions and data contained in all publications are solely those of the individual author(s) and contributor(s) and not of MDPI and/or the editor(s). MDPI and/or the editor(s) disclaim responsibility for any injury to people or property resulting from any ideas, methods, instructions or products referred to in the content.